Nano Research 2017, 10(5): 1584–1594
DOI 10.1007/s12274-016-1288-2
Research Article
ISSN 1998-0124
CN 11-5974/O4

Capping $CsPbBr_3$ with ZnO to improve performance and stability of perovskite memristors

Ye Wu[1,§], Yi Wei[1,§], Yong Huang[1], Fei Cao[1], Dejian Yu[1], Xiaoming Li[1,2] (✉), and Haibo Zeng[1,2] (✉)

[1] *Institute of Optoelectronics & Nanomaterials, Herbert Gleiter Institute of Nanoscience, Jiangsu Key Laboratory of Advanced Micro & Nano Materials and Technology, College of Material Science and Engineering, Nanjing University of Science and Technology, Nanjing 210094, China*

[2] *State Key Laboratory of Mechanics and Control of Mechanical Structures, College of Materials Science and Technology, Nanjing University of Aeronautics and Astronautics, Nanjing 210016, China*

[§] *These authors contributed equally to this work.*

Received: 20 July 2016
Revised: 7 September 2016
Accepted: 12 September 2016

KEYWORDS
inorganic perovskite,
bipolar resistive switching,
nonvolatile,
ZnO capping,
low power consumption

ABSTRACT

The rapid development of information technology has led to an urgent need for devices with fast information storage and processing, a high density, and low energy consumption. Memristors are considered to be next-generation memory devices with all of the aforementioned advantages. Recently, organometallic halide perovskites were reported to be promising active materials for memristors, although they have poor stability and mediocre performance. Herein, we report for the first time the fabrication of stable and high-performance memristors based on inorganic halide perovskite ($CsPbBr_3$, CPB). The devices have electric field-induced bipolar resistive switching (ReS) and memory behaviors with a large on/off ratio (>10^5), low working voltage (<1 V) and energy consumption, long data retention (>10^4 s), and high environmental stability, which are achieved via ZnO capping within the devices. Such a design can be adapted to various devices. Additionally, the heterojunction between the CPB and ZnO endows the devices with a light-induced ReS effect of more than 10^3 with a rapid response speed (<1 ms), which enables us to tune the resistance state by changing the light and electric field simultaneously. Such multifunctional devices achieved by the combination of information storage and processing abilities have potential applications for future computing that transcends traditional architectures.

1 Introduction

Since the invention of the computer, computer systems have been based on Von Neumann's theory, which consists of memory, computing, controlling, input, and output devices [1]. Among these, the memory and processor are key components. However, with the decrease of device size, silicon-based traditional

Address correspondence to Haibo Zeng, zeng.haibo@njust.edu.cn; Xiaoming Li, xml_mse@126.com

memory devices are reaching intrinsic limitations. Resistive random-access memory (RRAM) has been studied intensively over the past two decades and is considered to be a next-generation nonvolatile memory device owing to its advantages, including fast operation, favorable scalability, high density, and low power consumption [2, 3]. Importantly, when it is integrated with a complementary metal-oxide-semiconductor (CMOS), information storage and processing can be conducted within one device [4]. RRAM usually possesses a sandwich-like structure, which is built from a simple electrode/active material/electrode thin-film stack, and the active materials can be oxides [5–7], chalcogenides [8], and polymers [9, 10]. RRAMs with perovskite oxides, including $Pr_xCa_{1-x}MnO_3$ (PCMO), $BaTiO_3$, $SrTiO_3$, and $BiFeO_3$, have been successfully fabricated, including a 64-bit prototype device that was fabricated with PCMO [11–14]. However, ceramic perovskite oxide films usually have complicated components and are difficult to fabricate. Additionally, perovskite oxide films are incompatible with current CMOS processes.

Recently, a star-perovskite family—hybrid halide perovskites—has boosted the photon-conversion efficiency of corresponding solar cells to ~20% with advantages including fabrication convenience and low cost [15]. The superior optoelectronic properties of these materials endow them with potential applications beyond solar cells, such as photodetectors, light-emitting diodes, and lasing [16–19]. RRAMs based on such star-materials have been recently reported but have a small on/off ratio and high working current (high energy consumption) [19–22]. Additionally, the extreme sensitivity of hybrid halide perovskites to oxygen and moisture incurs the constraint of a critical environment for storage, fabrication, and operation. In contrast, the closely related inorganic halide perovskites (IPs), exhibit great potential for various applications owing to their ultrahigh photoluminescence quantum yield and better stability [23–25]. Owing to the similar crystal structure and electrical properties of IPs, it is possible to switch the resistance state (RS) with an electric field. Nevertheless, no research about RRAMs based on IPs has been reported thus far. Furthermore, although IPs are more stable than hybrid halide perovskites, problems such as sensitivity to moisture and the interface reaction between perovskite and metal electrodes remain, which hinder their practical applications [26]. The elaborate design of the device structure is urgently needed for improving the performance and stability.

Herein, we report for the first time the fabrication of memristors based on inorganic halide perovskite ($CsPbBr_3$, CPB) and their improvement of the stability and performance. The memristors possess nonvolatile bipolar resistive switching (ReS) and memory behaviors with instantaneous set/reset phenomena, a large on/off ratio (>10^5), a low working voltage (<1 V), long data retention (>10^4 s), and high environmental stability. These excellent characteristics were realized by capping the CPB film into a ZnO interlayer, which modified the film roughness and the contact of the CPB layer with the electrode, prevented interface reactions between the CPB and the metal electrode or moisture, and reduced the charge-carrier injection barrier and power consumption. Additionally, the device exhibited a light-induced ReS effect of more than 10^3 with a rapid response speed (<1 ms), which is highly reproducible and stable and enables us to tune their RS by using light and an electric field simultaneously. Such a multifunctional device achieved by the combination of information storage and processing abilities has potential for improved computing that transcends traditional architectures.

2 Results and discussion

To fabricate the memristor, CPB nanocrystal (NC) films were deposited on fluorine-doped tin oxide (FTO)/glass substrates by a centrifugal method and were treated according to our previous report [27]. The NCs had good crystallinity (Fig. S1 in the Electronic Supplementary Material (ESM)) and were stoichiometric (Fig. S2 in the ESM). Interestingly, the deposited films exhibited a strong orientation with the (002) planes, with a texture coefficient of 0.73 (detailed calculations can be found in Fig. S3 in the ESM). This is higher than that of randomly aggregated powders (0.52). The relatively high texture coefficient of the film indicates the textured and well-aligned features. Importantly, assembled films usually exhibit a high density and low roughness, which is beneficial for charge transport

and performance uniformity in optoelectronic and electronic devices (Fig. S4 in the ESM).

Although the IP has better stability than organometallic halide perovskites (OHPs), the ionic crystal feature makes them sensitive to moisture. To improve the device stability, a ZnO interlayer was introduced between the CPB and the electrode. ZnO, which exhibits ReS behavior when it is applied as the only active material, is a good candidate for memristors (Fig. 1(b)). The ZnO layer, which was amorphous, was sputtered at room temperature (Fig. S5 in the ESM). Compared with the previously reported direct deposition of ZnO, we scratched the surrounding parts of the as-prepared CPB film such that the CPB film was completely embedded in the ZnO, like a capping process , as shown in Fig. 1(c). To some extent, such a structure postpones the effect of moisture and interface reactions effectively and improves the device stability. The top cylindrical electrode was deposited by magnetron sputtering with a mask, and a schematic illustration is shown in Fig. 1(d). A relatively stable metal, Ni, was used as the top electrode. A cross-sectional scanning electron microscopy (SEM) image of a typical device is shown in Fig. 1(e), which indicates that the CPB layer is ~1 μm thick.

For the CPB-only device, when the voltage was swept from zero to a negative value, the current initially tended to increase, and a saltation process occurred at approximately −1.8 V (Fig. 2(a)), indicating ReS from an initial high-resistance state (HRS) to a low-resistance state (LRS). Subsequently, the voltage was swept from negative to positive, and the LRS remained until another resistance saltation from LRS to HRS occurred at ~2 V. At first, the ReS behavior at a reading voltage of 0.2 V was reversible, and both the HRS and LRS could be maintained. However, the device remained in the LRS for only ~10^3 s, exhibiting a very low stability (Fig. 2(b)) [28]. Although Ni is far more stable, it is insufficient for practical applications. When Ag was applied as the top electrode instead of Ni, the RS was found to be volatile (Fig. S6 in the ESM) owing to the direct contact of Ag^+ and X^- at the interface [26, 29]. Halide ions drifted toward the electrode under an external electric field, connecting the top and bottom electrodes. However, Ag reacted with halides because of the tight bonding of Ag and halide ions, forming AgX at the interface. Hence, the conductive path was interrupted, and the device switched to the HRS spontaneously [29].

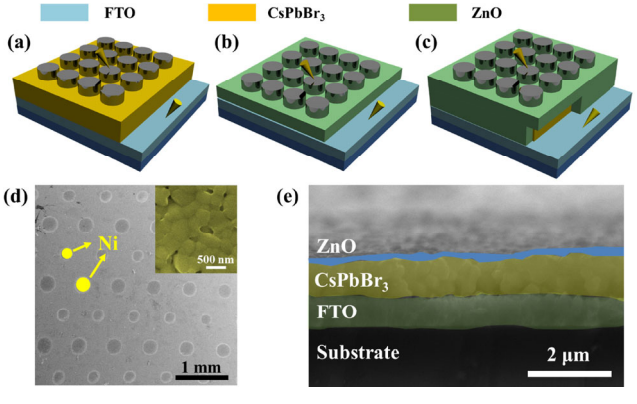

Figure 1 Device structures of three different memristors. Schematic of the (a) Ni/CPB/FTO, (b) Ni/ZnO/FTO, and (c) Ni/ZnO/CPB/FTO devices. (d) Surface SEM image of the device with nickel electrodes. (e) Cross-sectional SEM image of the device.

For the ZnO-only device, the reset process (ReS from HRS to LRS) represented a very typical negative differential resistance in the negative region, whereas the set process (ReS from LRS to HRS) occurring at ~1 V was instantaneous, which is consistent with our previous report (Fig. 2(c)) [30]. Importantly, the device exhibited outstanding stability, such that the RS was maintained for over 10^4 s and the on/off ratio remained at ~10^2 (Fig. 2(d)). This device also exhibited good reproducibility and reliable nonvolatile memory behavior up to 100 cycling times (Fig. S7 in the ESM). Therefore, the device stability is expected to be improved greatly with this interlayer, which inhibits the interaction between the CPB and metal electrode. Notably, when Pt or Au was applied as the top electrode, the on/off ratio was very small (Fig. S8 in the ESM). To explain this phenomenon, further investigations are needed. Figure 2(e) shows the current–voltage (*I*–*V*) curve of the ZnO capping device. The set process occurred at approximately −0.95 V, and the reset process occurred at ~0.71 V. These values are smaller than those for the CPB-only device and are among the best results. Both of the ReS behaviors were instantaneous. According to Fig. 2(f), the RS of the device was maintained for over 10^4 s at a reading voltage of 0.2 V, and the on/off ratio remained at ~10^5. These results indicate the high stability and good resistance retention after the introduction of the

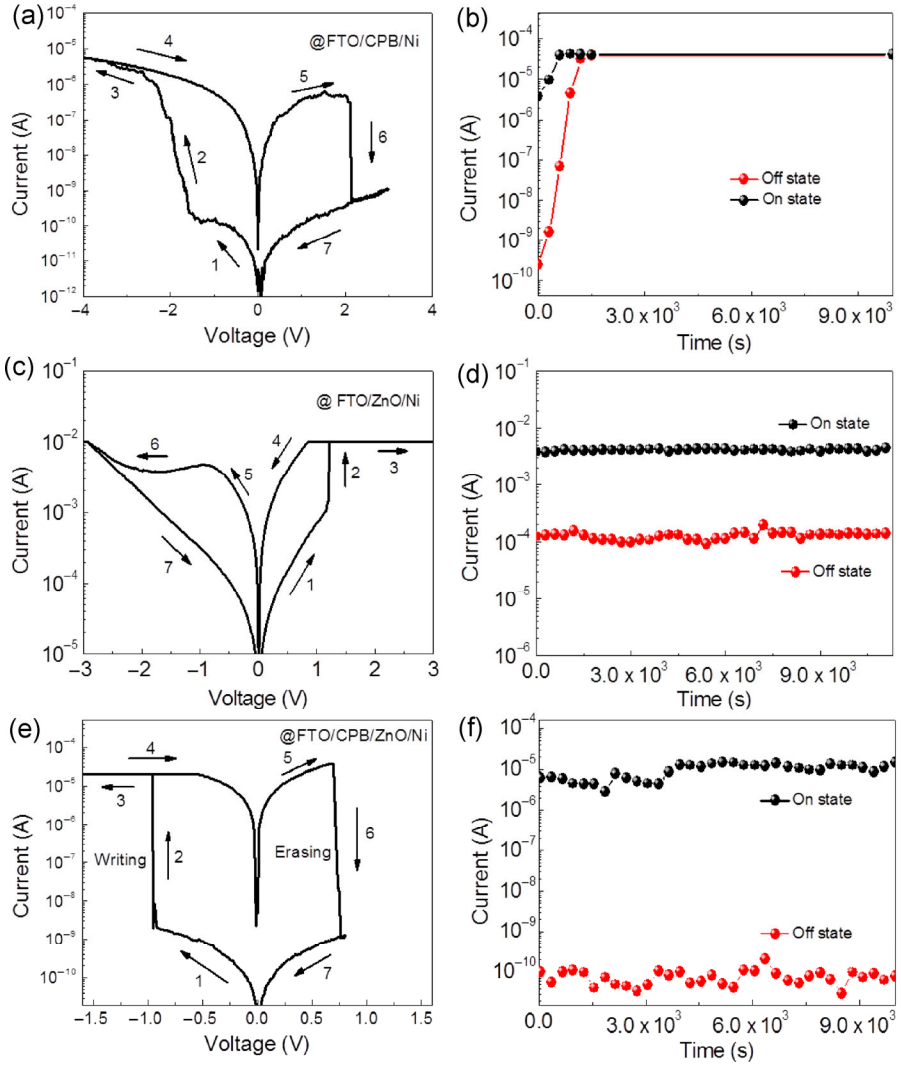

Figure 2 Device performances of three different memristors typical *I*–*V* curves and resistance-state stability of the three devices. (a) and (b) Ni/CPB/FTO, (c) and (d) Ni/ZnO/FTO, and (e) and (f) Ni/ZnO/CPB/FTO devices.

amorphous ZnO layer. Moreover, the RS was reversibly switched between the LRS and HRS by sweeping the voltage repeatedly more than 100 times between a negative value and a positive value, as shown in Fig. 3(a). The *I*–*V* curves show little difference from the first to last sweeping circle, indicating good endurance of the device performance. Furthermore, owing to the elaborate design, such a device structure prevents the direct contact of the CPB with air, reducing the influence of moisture on the CPB film. Therefore, the device exhibited good environmental stability compared with its hybrid competitor, such that after storage under ambient conditions, the device had a large on/off ratio for more than 20 days (Fig. 3(b)). The degradation after long-term storage might result from the influence of moisture, because after annealing at 100 ℃ for 30 min, a recovery was observed, and the performance remained constant for several days before complete damage.

The effect of the CPB film thickness, which is determined by the concentration of dispersions for centrifugal coating, as shown in Fig. S9 (in the ESM), was also investigated. The typical aforementioned device has the best performance when the set/reset voltages and on/off ratio are considered (Figs. S10 and S11 in the ESM). For traditional memristors, the active films are usually only several hundred nanometers thick; thinner films often result in a reduced

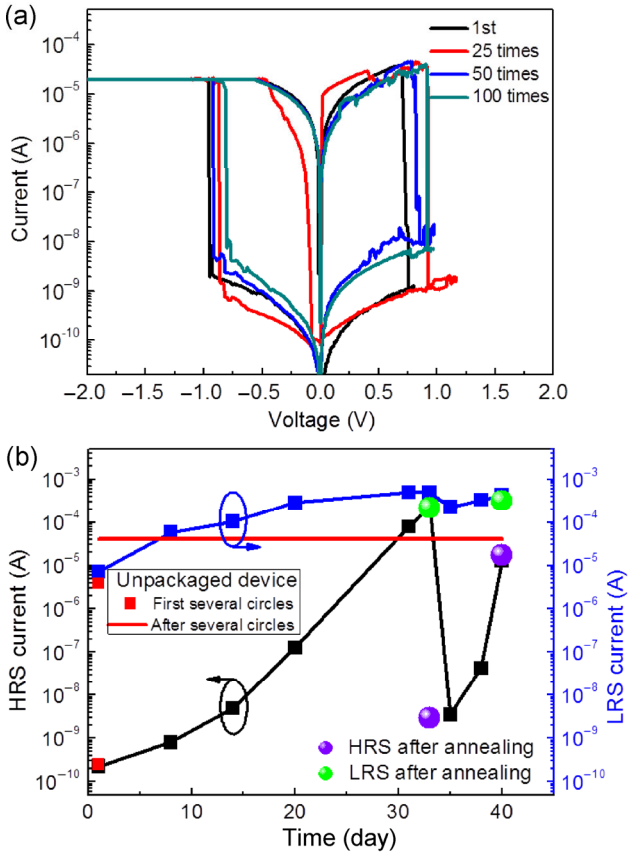

Figure 3 Performance and environmental stability of the device. (a) *I*–*V* characteristics at the first measurement and after different sweeping times up to 100. (b) On/off ratio of the device after long-term storage under ambient conditions. The stability performance of an uncapped device is also shown.

setting voltage. However, because of the lack of an effective film-deposition method and the inherent material characteristics, thin CPB films possess poor stability and frequently short-circuit. Thus, a better film-deposition strategy is needed. A thick film leads to a small on/off ratio owing to the enhanced film density and improved charge-transport ability.

Because no results regarding the RS behavior of inorganic halide perovskite have been reported, we compared our device with devices based on organic hybrid perovskites and perovskite oxides, as shown in Table 1. Our device exhibited lower set and reset voltages and a larger on/off ratio. In contrast, devices with other active materials usually have a small on/off ratio. Clearly, the designed structure endows our device with good environmental stability compared with devices based on OHPs. More importantly, for the bilayer device, the power consumption—a significant figure of merit for practical applications—is lowest and is two orders of magnitude lower than that in previous reports. The power consumption is calculated by multiplying the LRS current by the reading voltage [31]. Overall, the CPB film embedded in ZnO exhibited superior ReS behavior in many aspects.

To interpret the possible conduction mechanism, the negative part of the *I*–*V* curves were fitted according to different theories [38]. For the pure CPB device, the memristive behavior was dominated by ion drift [39], and the device with sole amorphous ZnO was dominated by Schottky emission, as reported in our previous work [30]. When Ag was applied as the

Table 1 Comparisons of the device performance between our memristors and those from recent reports regarding halide perovskites and perovskite oxides. The power consumption is defined as $P = CV$, where C is the current at a corresponding reading voltage (0.2 V)

Material	Set/reset voltage (V)	On/off ratio	Retention	LRS current	Power consumption	Refs.
$CsPbBr_3$/ZnO	**–0.95/+0.71**	**~10^5**	**>1 month**	**<10 μA**	**<10^{-6} W**	**This work**
$CH_3NH_3PbCl_xI_{3-x}$	+1.10/–1.65	~10^9	8 days	~10 mA	>10^{-2} W	[22]
$CH_3NH_3PbCl_xI_{3-x}$	+0.8/–0.6	<10	10^4 s	>1 mA	~2 × 10^{-4} W	[32]
$CH_3NH_3PbI_3$	+0.7/–0.5	<10^2	None	<1 mA	~10^{-4} W	[20]
$CH_3NH_3PbI_3$	–1/+2	>10^3	3 × 10^4 s	~1 mA	~2 × 10^{-4} W	[33]
$CH_3NH_3PbI_3$	+0.13/–0.15	~10^6	None	<1mA	<10^{-4} W	[34]
V-doped $SrZrO_3$	–13/+9	<10^3	None	>100 μA	~2 × 10^{-4} W	[21]
$Pr_{0.7}Ca_{0.3}MnO_3$	–0.75/+0.55	~10^2	None	<1 mA	~5 × 10^{-4} W	[35]
$SrTiO_3$	–1.7/+1.6	~10^4	None	<100 nA	~10^{-6} W	[36]
$CH_3NH_3PbCl_xI_{3-x}$	+1.5/–1.5	~10^3	4 × 10^4 s	<1 mA	<10^{-3} W	[37]

top electrode, the halide ions migrated directionally, connecting the top and bottom electrodes. However, Ag reacted with halide immediately, and the conductive filament was ruptured when the applied electronic field was removed, resulting in volatile ReS. For the ZnO capping device, fitting results suggest that the HRS region consisted of three conduction mechanisms—Ohmic conduction (0 to −0.125 V), Schottky emission (−0.125 to −0.61 V) and space-charge-limited current (SCLC, −0.61 to −0.95 V)—as shown in Fig. 4(a). For semiconductors, Ohm's law dominates the conductive mechanism at low voltages because intrinsic carriers contribute greatly to the conduction. The *I*–*V* curve in this region shows linear Ohmic conductive behavior with a slope of 9.4×10^{-10} S (Fig. 4(b)), indicating a resistance higher than 1 GΩ for the off state. However, when the negative voltage scans forward, the *I*–*V* curve becomes nonlinear. The voltages ranging from −0.125 to −0.61 V were re-plotted in ln*I*–$V^{1/2}$ versions (Fig. 4(c)) and showed a clear agreement with the results. This suggests that a Schottky emission was boosted to inject charges from the Ni electrode to the ZnO/CPB interface, which can be described by the following equation

$$\ln I \propto \sqrt{\frac{e^3}{4\pi\varepsilon_0\varepsilon_r d}} KT \cdot \sqrt{V}$$

Here, I is the current, V is the applied voltage, e is the electronic charge, K is the Boltzmann's constant, ε_0 is the permittivity of free space, ε_r is the relative dielectric constant, and T is the temperature. For an increasing voltage in the range of −0.61 to −0.95 V, the current was fitted linearly as a function of V^2 (Fig. 4(d)), indicating that the conduction mechanism follows the SCLC model. The relationship between the current and voltage of the trap-filled SCLC can be described as follows

$$J = \frac{8}{9}\varepsilon_0\varepsilon_r\mu\frac{E^2}{d^3}$$

Here, J is the current density, μ is the mobility of the charge carriers, E is the electric field, and d is the film thickness. The SCLC conduction in the *I*–*V* curve indicates that charge-trapping levels resulting from defects may have formed in the perovskite layer [40].

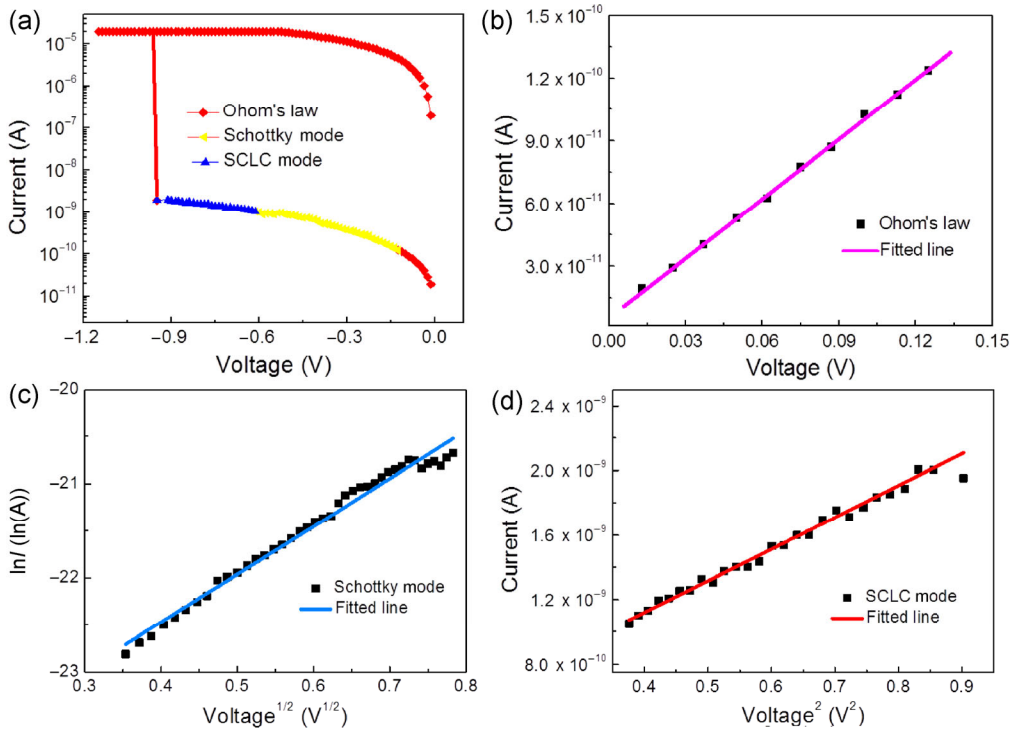

Figure 4 Conduction mechanism of the bilayer device. (a) Re-plotted negative part of the switching *I*–*V* curve. (b) *I*–*V*, (c) ln*I*–$V^{1/2}$, and (d) *I*–V^2 curves for Ohmic, Schottky, and SCLC conduction mechanisms. The straight line shows the linear fitting.

Subsequently, the current increased, switching the device from an HRS to an LRS at −0.95 V. The LRS region (−1.2 ~ 0 V) exhibits linear conduction behavior similar to Ohm's Law, as shown in Fig. S12 (in the ESM). This phenomenon can be explained by the reduction of the Schottky barrier width in the vicinity of the interface, which allowed electrons to pass through the thin barrier via a tunneling process [2]. The LRS region could not be dominated by Ohm's Law, because the conductive carriers were leaping charges rather than a metal filament.

Obviously, both the Schottky emission and SCLC model had indispensable effects on the bilayer ReS device. Thus, a simplified physical model was proposed to explain the improved ReS effect, as shown in Fig. 5. At the initial state (low-bias region), as there was no extra bias, all three devices exhibited an HRS owing to the barrier on the perovskite/metal (ZnO). For the pure CPB device, with the increase of negative bias, only ion drift contributed to the conduction. Hence, a large set voltage was observed, and the ReS was not instantaneous. This was confirmed by the results for the device with a Pt electrode (Fig. S7 in the ESM).

For the modified device, when the negative bias was applied, electrons were injected into the compact ZnO layer by Schottky emission, and a barrier existed in the interface of CPB/ZnO. In the low-bias region, because the electric field was too small for electrons to jump over the barrier, the electrons were bound by traps, forming trapping centers and keeping the device in a considerable HRS (Fig. 5(a)). As the negative bias was increased, the existing trapping centers were gradually occupied by injected carriers. Excess electrons accumulated near the interface of CPB/ZnO, forming a space charge and increasing the energy of the system. To neutralize this trend, a built-in field was created to hinder further injection [41]. Hence, the *I*–*V* curve became mild, matching Child's law ($I \propto V^2$). When a negative bias larger than −0.95 V was applied, which is nearly equal to the energy-level difference between the CBM of perovskite and the work function of the Ni electrode, the excessive electrons achieved enough energy to jump over the barrier abruptly, switching the device to an LRS instantaneously (Fig. 5(b)). Even when the electric field was removed, the LRS remained, owing to the charge-trapping ability of the CPB film. When a positive bias was applied, the charges were extracted, resulting in an HRS. This process was reversible and stable.

The compact ZnO layer played an important role in the injection and extraction of electrons. The introduction of ZnO completely changed the ReS mechanism from ion drift to Schottky emission and the SCLC model. First, the compact ZnO layer effectively blocked the channel for ionic migration, and charge injection played a dominant role in the carrier transport. ZnO offered a headstone for electron jumping between the perovskite and the metal electrode, reducing the injection barrier [42]. Consequently, a lower set voltage was achieved compared with the device without the ZnO layer. The high electron conductivity of the ZnO layer enabled charge carriers to be ejected easily under a small positive voltage, switching the device to an HRS. A far smaller reset

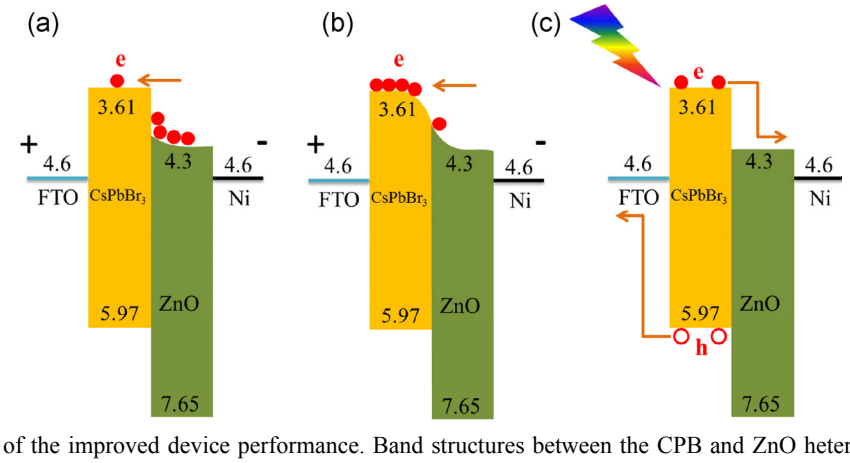

Figure 5 Mechanism of the improved device performance. Band structures between the CPB and ZnO heterojunction at (a) low and (b) large negative biases. (c) Photogeneration and extraction of carriers without any bias for light-induced resistive switching.

voltage was observed with a positive bias, which accords with the difference in the energy level between ZnO and perovskite, indicating that once the electrons were dropped from the CBM of perovskite to that of ZnO, the conductive path disappeared. Second, the ZnO layer contributed significantly to the instantaneous resistive switching. By adding a ZnO layer, excessive electrons were gathered near the interface, and they then jumped directly from the CBM of ZnO to that of CPB, instead of being gradually occupied by traps in the perovskite. Therefore, compared with the FTO/CPB/ZnO/Ni device, the FTO/CPB/Ni device showed no Schottky emission process and no instantaneous set behavior. In contrast, in the higher-voltage region, the current of the HRS increased very quickly, corresponding to the steep increase [43]. Finally, the ZnO layer prevented the device from being broken down via the interface reaction of CPB and Ni (resulting from charge stacking) and modified the CPB film roughness and the contact of the perovskite layer with the electrode, ensuring the stable behavior and circle endurance.

According to the energy-band alignment of ZnO and CPB, a heterojunction was formed at the interface, and the internal field enabled charge separation without an external bias (Fig. 5(c)). Therefore, the photovoltaic device can operate by itself under illumination. Additionally, the lower valence-band energy of ZnO can block the separated holes, ensuring efficient electron/hole transport and extraction. That is, the device exhibits ReS behavior in the dark and under illumination. Figure 6(a) shows the *I*–*V* curves in the dark and under illumination of continuous-wave monochromatic light (442 nm, 1.01 mW·cm^{-2}) under ambient conditions. As expected, in the dark, the device remained in the HRS. The current increased rapidly upon illumination, resulting in an on/off ratio of ~10^3. The sweeping of the voltage from negative to positive did not induce a resistance change, and the ReS behavior was observed within the sweeping region.

Upon irradiation, the photocurrent increased sharply, and when the light was removed, the current decreased quickly (Fig. 6(b)). The periodic response to light is shown in Fig. 4(e), indicating that the device has excellent stability. The response time was investigated using a continuous-wave 442-nm laser assisted by a

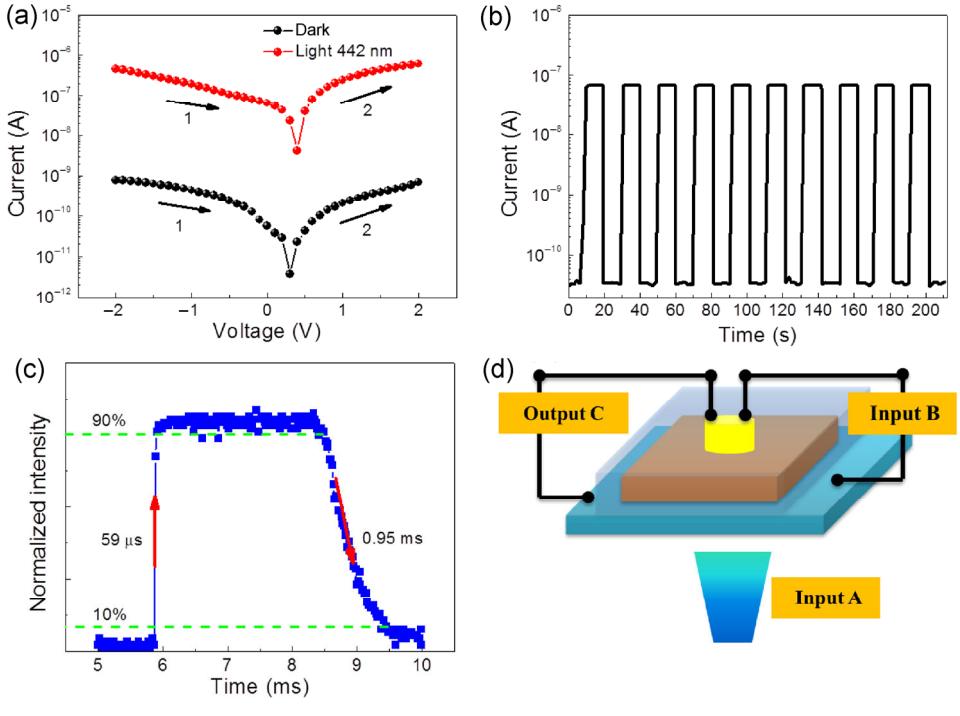

Figure 6 Photovoltaic behavior of the device. (a) Logarithmic *I*–*V* curves of the bilayer device measured in the dark and under light at the wavelength of 442 nm (1.01 mW·cm^{-2}). (b) *I*–*t* curves of the device at 0 V. (c) Resistive switching speed of the device at a light intensity of 1.01 mW·cm^{-2}. (d) Schematic of the logic-gate device with two input signals and one output signal.

trigger with a tunable pulse width. The rise time and decay time were extracted as 59 μs and 0.95 ms, respectively, under a pulse width of 200 Hz (Fig. 6(c)), indicating the fast ReS behavior of the device. Such a high response speed and responsivity ensure the efficient communication of information (Fig. S13 in the ESM).

As the resistance of the bilayer device can be switched between high and low states driven by both light and electricity, a logic "OR" gate was designed, as shown in Fig. 6(d), which can process and store information simultaneously. We define the light and electricity as input signals A and B, respectively. C is the output signal. We define the current for the light turned ON and the LRSs as signal "1" and the current for the light turned OFF and the HRSs as signal "0", as described in the table of Fig. S14 in the ESM. Accordingly, the high-current level is "1" and the low-current level is "0" for the output signal C. Consequently, if one of the inputs is a "1" signal, the device output is always a "1" signal. Only if both of the inputs are "0" signals is the output signal "0". This bilayer device can implement logic operations as an "OR" logic gate. The photocurrent and dark current were on the same order of magnitude as the currents of the LRS and HRS, leading to a small possibility of misreading.

3 Conclusion

We report the fabrication of memristors based on IP (CPB) and their improvement of the device stability and performance. The modified device shows nonvolatile bipolar resistive switching and memory effects with instantaneous set/reset phenomena, a large on/off ratio (>10^5), a low operation voltage (<1 V), long data retention (>10^4 s), and high environmental stability. These excellent characteristics were achieved by introducing a ZnO interlayer between the CPB and the metal electrode, i.e., embedding the CPB layer completely. The results reveal that IPs not only exhibit impressive ReS behavior at a low working voltage and good stability but also possess advantages of solution and room-temperature processability for flexible devices. They are hence promising candidates for nonvolatile memory devices. Additionally, a light-induced ReS effect of more than 10^3 with a rapid response speed (<1 ms) enables information storage and processing to be conducted simultaneously, indicating potential for improved computing that transcends traditional architectures.

4 Method

The $CsPbBr_3$ NC dispersion was synthesized according to our previous reports, with modifications [25]. Briefly, CsBr (0.213 g) and $PbBr_2$ (0.369 g) were dissolved in a mixture of DMSO (10 mL) and hydrobromic acid (10 μL, 40% in water). Oleic acid (OA) (1 mL) and oleylamine (OAm) (0.2 mL) were added in order to stabilize the precursor solution. Then, 2 mL of the precursor solution were injected into 100 mL of toluene swiftly under vigorous stirring at room temperature. The $CsPbBr_3$ film was centrifuged onto a pre-cleaned commercial FTO substrate (sheet resistance ~7 $\Omega \cdot sq^{-1}$), and the film thickness was controlled by changing the centrifugal speed and concentration. After treatment with a room-temperature film-healing strategy based on our previous work [27], a compact and amorphous ZnO layer was deposited above the perovskite films by radio frequency (RF) magnetron sputtering. The detailed deposition parameters are presented in our previous work [30]. Circle-shaped Ni electrodes were deposited with a shadow mask via magnetron sputtering. For a typical device, the thicknesses of $CsPbBr_3$, ZnO, and Ni were ~1,000, 100, and 100 nm, respectively.

X-ray diffraction (XRD) measurements were performed with a Bruker D8 Advance XRD system. Transmission electron microscopy (TEM) and high-resolution TEM images were measured with FEI Tecnai G20 on a Cu grid. SEM images of the films and the device cross sections were obtained using a field-emission electron microscope (Quanta 250F, FEI). X-ray photoelectron spectroscopy analysis was performed using an ARL-9800 instrument with monochromatic X-ray Al Kα excitation (1,486.6 eV). The current–voltage characteristics of the devices were measured at room temperature in air using a semiconductor characterization system (Keithley 4200). The device endurance was examined by the voltage sweep mode. The retention characteristics were investigated up to ~10^4 s with a reading voltage of 0.2 V.

Acknowledgements

This work was financially supported by National Basic Research Program of China (No. 2014CB931702), National Natural Science Foundation of China (Nos. 51572128 and 5151101197), and the Priority Academic Program Development of Jiangsu Higher Education Institutions (PAPD).

Electronic Supplementary Material: Supplementary material is available in the online version of this article at http://dx.doi.org/10.1007/s12274-016-1288-2.

References

[1] von Neumann, J. First draft of a report on the EDVAC. In *The Origins of Digital Computers: Selected Papers*; Randell, B., Ed.; Springer: Berlin Heidelberg, 1982; pp 383–392.

[2] Sawa, A. Resistive switching in transition metal oxides. *Mater. Today* **2008**, *11*, 28–36.

[3] Pan, F.; Gao, S.; Chen, C.; Song, C.; Zeng, F. Recent progress in resistive random access memories: Materials, switching mechanisms, and performance. *Mater. Sci. Eng. R* **2014**, *83*, 1–59.

[4] Xia, Q. F.; Robinett, W.; Cumbie, M. W.; Banerjee, N.; Cardinali, T. J.; Yang, J. J.; Wu, W.; Li, X. M.; Tong, W. M.; Strukov, D. B. et al. Memristor−CMOS hybrid integrated circuits for reconfigurable logic. *Nano Lett.* **2009**, *9*, 3640–3645.

[5] Song, S. J.; Seok, J. Y.; Yoon, J. H.; Kim, K. M.; Kim, G. H.; Lee, M. H.; Hwang, C. S. Real-time identification of the evolution of conducting nano-filaments in TiO_2 thin film ReRAM. *Sci. Rep.* **2013**, *3*, 3443.

[6] Chen, C.; Song, C.; Yang, J.; Zeng, F.; Pan, F. Oxygen migration induced resistive switching effect and its thermal stability in W/TaO_x/Pt structure. *Appl. Phys. Lett.* **2012**, *100*, 253509.

[7] Chen, G.; Song, C.; Chen, C.; Gao, S.; Zeng, F.; Pan, F. Resistive switching and magnetic modulation in cobalt-doped ZnO. *Adv. Mater.* **2012**, *24*, 3515–3520.

[8] Jang, J.; Pan, F.; Braam, K.; Subramanian, V. Resistance switching characteristics of solid electrolyte chalcogenide Ag_2Se nanoparticles for flexible nonvolatile memory applications. *Adv. Mater.* **2012**, *24*, 3573–3576.

[9] Carchano, H.; Lacoste, R.; Segui, Y. Bistable electrical switching in polymer thin films. *Appl. Phys. Lett.* **1971**, *19*, 414–415.

[10] Pender, L. F.; Fleming, R. J. Memory switching in glow discharge polymerized thin films. *J. Appl. Phys.* **1975**, *46*, 3426–3431.

[11] Kaji, H.; Kondo, H.; Fujii, T.; Arita, M.; Takahashi, Y. Effect of electrode and interface oxide on the property of ReRAM composed of $Pr_{0.7}Ca_{0.3}MnO_3$. *IOP Conf. Ser.: Mater. Sci. Eng.* **2010**, *8*, 012032.

[12] Wang, L.; Jin, K.-J.; Ge, C.; Wang, C.; Guo, H.-Z.; Lu, H.-B.; Yang, G.-Z. Electro-photo double modulation on the resistive switching behavior and switchable photoelectric effect in $BiFeO_3$ films. *Appl. Phys. Lett.* **2013**, *102*, 252907.

[13] Jia, C. H.; Sun, X. W.; Li, G. Q.; Chen, Y. H.; Zhang, W. F. Origin of attendant phenomena of bipolar resistive switching and negative differential resistance in $SrTiO_3$:Nb/ZnO heterojunctions. *Appl. Phys. Lett.* **2014**, *104*, 043501.

[14] Sekhar, K. C.; Silva, J. P. B.; Kamakshi, K.; Pereira, M.; Gomes, M. J. M. Semiconductor layer thickness impact on optical and resistive switching behavior of pulsed laser deposited $BaTiO_3$/ZnO heterostructures. *Appl. Phys. Lett.* **2013**, *102*, 212903.

[15] Yang, W. S.; Noh, J. H.; Jeon, N. J.; Kim, Y. C.; Ryu, S.; Seo, J.; Seok, S. I. High-performance photovoltaic perovskite layers fabricated through intramolecular exchange. *Science* **2015**, *348*, 1234–1237.

[16] Hu, X.; Zhang, X. D.; Liang, L.; Bao, J.; Li, S.; Yang, W. L.; Xie, Y. High-performance flexible broadband photodetector based on organolead halide perovskite. *Adv. Funct. Mater.* **2014**, *24*, 7373–7380.

[17] Tan, Z.-K.; Moghaddam, R. S.; Lai, M. L.; Docampo, P.; Higler, R.; Deschler, F.; Price, M.; Sadhanala, A.; Pazos, L. M.; Credgington, D. et al. Bright light-emitting diodes based on organometal halide perovskite. *Nat. Nanotechnol.* **2014**, *9*, 687–692.

[18] Wang, Y.; Li, X. M.; Song, J. Z.; Xiao, L.; Zeng, H. B.; Sun, H. D. All-inorganic colloidal perovskite quantum dots: A new class of lasing materials with favorable characteristics. *Adv. Mater.* **2015**, *27*, 7101–7108.

[19] Huang, H.; Susha, A. S.; Kershaw, S. V.; Hung, T. F.; Rogach, A. L. Control of emission color of high quantum yield $CH_3NH_3PbBr_3$ perovskite quantum dots by precipitation temperature. *Adv. Sci.* **2015**, *2*, 1500194.

[20] Gu, C. W.; Lee, J.-S. Flexible hybrid organic–inorganic perovskite memory. *ACS Nano* **2016**, *10*, 5413–5418.

[21] Lin, C. C.; Tu, B. C.; Lin, C. H.; Lin, C. H.; Tseng, T. Y. Resistive switching mechanisms of V-doped $SrZrO_3$ memory films. *IEEE Elec. Dev. Lett.* **2006**, *27*, 725–727.

[22] Yan, K.; Peng, M.; Yu, X.; Cai, X.; Chen, S.; Hu, H. W.; Chen, B. X.; Gao, X.; Dong, B.; Zou, D. C. High-performance perovskite memristor based on methyl ammonium lead halides. *J. Mater. Chem. C* **2016**, *4*, 1375–1381.

[23] Wang, Y.; Li, X. M.; Zhao, X.; Xiao, L.; Zeng, H. B; Sun, H. D. Nonlinear absorption and low-threshold multiphoton pumped stimulated emission from all-inorganic perovskite nanocrystals. *Nano Lett.* **2016**, *16*, 448–453.

[24] Song, J. Z.; Li, J. H.; Li, X. M.; Xu, L. M.; Dong, Y. H.; Zeng, H. B. Quantum dot light-emitting diodes based on inorganic perovskite cesium lead halides ($CsPbX_3$). *Adv. Mater.* **2015**, *27*, 7162–7167.

[25] Li, X. M.; Wu, Y.; Zhang, S. L.; Cai, B.; Gu, Y.; Song, J. Z.; Zeng, H. B. $CsPbX_3$ quantum dots for lighting and displays: Room-temperature synthesis, photoluminescence superiorities, underlying origins and white light-emitting diodes. *Adv. Funct. Mater.* **2016**, *26*, 2435–2445.

[26] Lee, K.-T.; Guo, L. J.; Park, H. J. Neutral- and multi-colored semitransparent perovskite solar cells. *Molecules* **2016**, *21*, 475.

[27] Li, X. M.; Yu, D. J.; Cao, F.; Gu, Y.; Wei, Y.; Wu, Y.; Song, J. Z.; Zeng, H. B. Healing all-inorganic perovskite films via recyclable dissolution-recyrstallization for compact and smooth carrier channels of optoelectronic devices with high stability. *Adv. Funct. Mater.* **2016**, *26*, 5903–5912.

[28] Han, Y.; Meyer, S.; Dkhissi, Y.; Weber, K.; Pringle, J. M.; Bach, U.; Spiccia, L.; Cheng, Y.-B. Degradation observations of encapsulated planar $CH_3NH_3PbI_3$ perovskite solar cells at high temperatures and humidity. *J. Mater. Chem. A* **2015**, *3*, 8139–8147.

[29] Kato, Y. C.; Ono, L. K.; Lee, M. V.; Wang, S. H.; Raga, S. R.; Qi, Y. B. Silver iodide formation in methyl ammonium lead iodide perovskite solar cells with silver top electrodes. *Adv. Mater. Interfaces* **2015**, *2*, 1500195.

[30] Huang, Y.; Shen, Z. H.; Wu, Y.; Wang, X. Q.; Zhang, S. F.; Shi, X. Q.; Zeng, H. B. Amorphous ZnO based resistive random access memory. *RSC Adv*. **2016**, *6*, 17867–17872.

[31] Fan, Y. S.; Liu, P. T. Characteristic evolution from rectifier Schottky diode to resistive-switching memory with Al-doped zinc tin oxide film. *IEEE Trans. Elec. Dev.* **2014**, *61*, 1071–1076.

[32] Yoo, E. J.; Lyu, M. Q.; Yun, J.-H.; Kang, C. J.; Choi, Y. J.; Wang, L. Z. Resistive switching behavior in organic–inorganic hybrid $CH_3NH_3PbI_{3-X}Cl_X$ perovskite for resistive random access memory devices. *Adv. Mater.* **2015**, *27*, 6170–6175.

[33] Lin, G. M.; Lin, Y. W.; Cui, R. L.; Huang, H.; Guo, X. H.; Li, C.; Dong, J. Q.; Guo, X. F.; Sun, B. Q. An organic-inorganic hybrid perovskite logic gate for better computing. *J. Mater. Chem. C* **2015**, *3*, 10793–10798.

[34] Choi, J.; Park, S.; Lee, J.; Hong, K.; Kim, D.-H.; Moon, C. W.; Park, G. D.; Suh, J.; Hwang, J.; Kim, S. Y. et al. Organolead halide perovskites for low operating voltage multilevel resistive switching. *Adv. Mater.* **2016**, *28*, 6562–6567.

[35] Kim, I.; Siddik, M.; Shin, J.; Biju, K. P.; Jung, S.; Hwang, H. Low temperature solution-processed graphene oxide/$Pr_{0.7}Ca_{0.3}MnO_3$ based resistive-memory device. *Appl. Phys. Lett*. **2011**, *99*, 042101.

[36] Kim, C. H.; Ahn, Y.; Son, J. Y. $SrTiO_3$-based resistive switching memory device with graphene nanoribbon electrodes. *J. Am. Ceram. Soc.* **2016**, *99*, 9–11.

[37] Yoo, E.; Lyu, M. Q.; Yun, J.-H.; Kang, C. J.; Choi, Y.; Wang, L. Z. Bifunctional resistive switching behavior in an organolead halide perovskite based Ag/$CH_3NH_3PbI_{3-x}Cl_x$/FTO structure. *J. Mater. Chem. C* **2016**, *4*, 7824–7830.

[38] Szmytkowski, J. The influence of the thickness, recombination and space charge on the loss of photocurrent in organic semiconductors: An analytical model. *J. Phys. D: Appl. Phys*. **2007**, *40*, 3352.

[39] Xiao, Z. G.; Yuan, Y. B.; Shao, Y. C.; Wang, Q.; Dong, Q. F.; Bi, C.; Sharma, P.; Gruverman, A.; Huang, J. S. Giant switchable photovoltaic effect in organometal trihalide perovskite devices. *Nat. Mater.* **2015**, *14*, 193–198.

[40] Shi, D.; Adinolfi, V.; Comin, R.; Yuan, M. J.; Alarousu, E.; Buin, A.; Chen, Y.; Hoogland, S.; Rothenberger, A.; Katsiev, K. et al. Low trap-state density and long carrier diffusion in organolead trihalide perovskite single crystals. *Science* **2015**, *347*, 519–522.

[41] Lin, C.-Y.; Wang, S.-Y.; Lee, D.-Y.; Tseng, T.-Y. Electrical properties and fatigue behaviors of ZrO_2 resistive switching thin films. *J. Electrochem. Soc.* **2008**, *155*, H615–H619.

[42] Qian, L.; Zheng, Y.; Xue, J. E.; Holloway, P. H. Stable and efficient quantum-dot light-emitting diodes based on solution-processed multilayer structures. *Nat. Photonics* **2011**, *5*, 543–548.

[43] Liu, Q.; Guan, W. H.; Long, S. B.; Jia, R.; Liu, M.; Chen, J. N. Resistive switching memory effect of ZrO_2 films with Zr^+ implanted. *Appl. Phys. Lett.* **2008**, *92*, 012117.